Complementing and Validating Uncertainty of Terrestrial Laser Scanning via Interval Analysis

Reza Naeimaei[1,*], Steffen Schön[1]

[1] Institut für Erdmessung (IfE), Leibniz University Hannover, Hannover, Germany
(naeimaei@ife.uni-hannover.de, schoen@ife.uni-hannover.de)

Keywords: Terrestrial laser scanning, Uncertainty budget, Uncertainty propagation, Interval analysis, Deformation monitoring, Gauss–Helmert model

Abstract

Terrestrial laser scanning (TLS) enables dense spatial sampling. However, the analysis of millimeter-level deformations is limited by uncertainty rather than resolution. Inter-epoch differences can arise from actual changes or systematic effects. Classical stochastic models address random variability based on certain distributional assumptions, but they do not offer deterministic bounds for persistent effects that remain even after calibration and correction. This paper presents a complementary interval-based framework for bounding such effects and integrating them into least-squares workflows. Starting from measurement and instrumental correction models for high-end panoramic scanners, bounded deviations of influence parameters are propagated to TLS observations and represented as observation-level interval radii. These radii are then mapped via an interval-extended least-squares adjustment to obtain conservative bounds on residuals and parameter estimates, along with stochastic covariances. To validate the interval description without a trusted nominal reference, we propose a residual-domain strategy based on two-face (Face 1/Face 2) acquisitions. In this strategy, the model parameters are first estimated from Face 1 observations and then kept fixed when evaluating the corresponding Face 2 observations. This prevents the adjustment from absorbing remaining systematic effects into the model parameters. The resulting averaged face-combined residuals are then compared with the propagated interval bounds. The approach is demonstrated on real TLS data from the Bonn reference wall. The results show that the propagated bounds generally enclose the averaged face-combined residuals and reveal station-dependent residual structures that motivate extending the current instrument-only interval budget to include geometry, registration, and surface-interaction effects.

1. Introduction

Deformation monitoring of natural and human-made structures is a key focus of engineering geodesy (Kuhlmann et al., 2014). This includes landslides and rockfalls as well as bridges, dams, tunnels, and other critical infrastructure. In this regard, terrestrial laser scanning (TLS) has become increasingly important because it can reliably detect centimetre-scale geometric change. At the millimetre-scale, however, differences between point clouds from two epochs may indicate either true deformation or remaining effects within the data. Disentangling these sources requires a rigorous treatment of measurement uncertainty.

To address this challenge, precise geodetic engineering depends on a clear understanding of sensor performance and uncertainty. Because many error sources interact, for instance, measurement geometry and object properties are interconnected, as both affect how the laser beam interacts with the measured object (Medić, 2021). A recent notable contribution is the comprehensive Elementary Error Model (EEM) by Kerekes (Kerekes, 2023). The EEM introduces a stochastic model for TLS observations that groups error sources into classes and analyses their origins. However, in practical monitoring campaigns, it remains challenging to establish a complete, task-specific uncertainty budget for TLS point clouds that also accounts for object (and scene) dependent influences and remaining systematic effects after applying state-of-the-art correction models (Jost, 2023). In operational TLS deformation monitoring, uncertainty is commonly represented by a variance–covariance matrix (VCM), and congruency tests based on the VCM are used to distinguish observation error from true change (Caspary et al., 1987; Heunecke et al., 2013). While this stochastic description is well suited to representing random variability through variances and covariances, it does not by itself provide deterministic bounds for persistent remaining systematic effects. This motivates interval-based uncertainty bounds and their propagation as a complementary description.

A complementary framework for this purpose is *interval analysis*. Interval methods provide guaranteed, bounded-error descriptions of quantities and support their propagation through mathematical models. Originally developed to rigorously bound rounding errors in scientific computation (Alefeld and Herzberger, 1983), interval analysis has since been applied in robust estimation and robotics, including set-based localization and sensor fusion (Jaulin et al., 2001). In these applications, intervals enclose maximum observation errors and propagate these bounds through measurement and estimation models.

Beyond robotics and control, interval analysis has a notable history in geodesy. Early work employed min–max tolerating to handle measurement bounds (Reinhart, 1975), later refined via interval least-squares estimators and the integration of fuzzy sets (Kutterer, 1994), with applications to deformation-network optimization (Schön and Kutterer, 2006). For Global Navigation Satellite Systems (GNSS), observation intervals that account for ionospheric refraction and multipath have been derived and validated on extensive real-world data (Su and Schön, 2022). Despite these advances, rigorous and practically meaningful bounds for TLS observation intervals remain underexplored. To address this gap, we propose an interval-based approach for deriving TLS uncertainty bounds that explicitly incorporates systematic effects while modelling random variability as a normally distributed random variable. This strengthens TLS uncertainty management, which is critical for accurate deformation analysis.

This contribution has been peer-reviewed. The double-blind peer-review was conducted on the basis of the full paper.
https://doi.org/10.5194/isprs-annals-XI-1-2026-391-2026

Expanding on this topic, in our previous studies (Naeimaei and Schön, 2025; Naeimaei and Schön, 2025) we introduced the interval framework that identifies influence parameters and performs a sensitivity analysis of the TLS measurement and correction models. The resulting observation intervals enclose remaining systematic deviations and are linearly propagated to Cartesian coordinates for both simulated and real observations, yielding a deterministic interval-based uncertainty description. Building on this foundation, the main contributions of this article are:

- **Interval-based uncertainty budget:** Propagation of instrumental parameter deviations to the observation domain to obtain interval bounds enclosing remaining systematic effects.
- **Interval-extended adjustment:** Transfer of interval propagation into the least-squares adjustment, providing conservative first-order enclosures for residuals and parameter estimates alongside stochastic covariances.
- **Reference-free validation strategy:** A residual-based validation concept using two-face measurements, eliminating the need for a superior nominal reference.
- **Application to real data:** Demonstration on real TLS data, illustrating separation of random variability from persistent systematic biases.

The remainder of the paper is organized as follows. Section 2 presents the two-face design and residual-based validation concept, the TLS measurement/correction model, and interval propagation within the Gauss–Helmert model. Section 3 describes the Bonn reference wall experiment, data acquisition, and registration. Section 4 reports the validation results, including station/component-wise assessments and residual trend/spatial-pattern diagnostics. Conclusions and an outlook are given in Section 5.

2. Methodology

2.1 Dealing with uncertainty

In this work, *uncertainty* characterizes the dispersion of values that could reasonably be attributed to a measurement and is conceptually distinct from *error*, the difference between a measured value and the (unknowable) true value (BIPM et al., n.d.). Because the true value cannot be determined exactly, uncertainty is the more practical quantity for reporting and decision-making.

For TLS applications, we distinguish two principal contributors to uncertainty: (i) random variability, commonly modeled stochastically (e.g., assuming a normal distribution), and (ii) uncertainty about remaining systematic effects that persist after calibration and corrections. While the former is naturally handled by probabilistic models, the latter is better represented by bounded sets. Accordingly, we adopt an *interval* description for bounding residual systematic effects. Figure 1 illustrates the idea in one dimension. The difference between the sample mean and an external reference indicates a remaining systematic error; our goal is to bound such effects by an interval around the mean. The corresponding *interval radii* (Δ) are computed via sensitivity analysis (Section 2.4) and propagated through the TLS model (Section 2.5). We denote intervals by their lower and upper bounds, $[a] = [\underline{a}, \overline{a}] = [a_m - \Delta, a_m + \Delta]$; see Jaulin et al. (2001); Moore et al. (2009) for comprehensive introductions to interval computation.

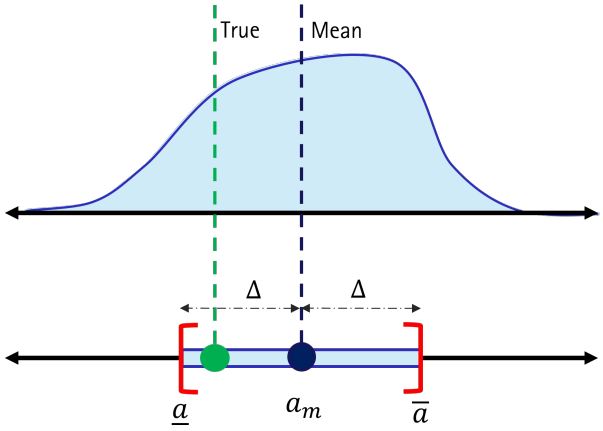

Figure 1. Conceptual one-dimensional uncertainty. The upper sketch shows a probability density function with the sample mean (blue dashed line). A green dashed line shows the ”true” value; the offset between the reference and the sample mean indicates a remaining systematic error. Additionally, the horizontal bar illustrates an interval centered at the mean that encloses the remaining systematic effects.

2.2 Validating the interval-based uncertainty description

Since both random and remaining systematic uncertainty components are present in TLS measurements, they have to be separated for validation. For the random part, the underlying probability distribution of the observation noise is the reference, cf. Figure 1. This includes that this part can only be described as expectation, having multiple observations at hand, e.g., as a sample mean value, by a histogram approximating the assumed probability distribution, or by a confidence interval enclosing the observations with a certain probability. Subsequently, it is hard to make a statement for a single observation.

Figure 1 illustrates the idea of validating interval bounds against real data: an interval encloses the remaining systematics around a mean value. and thus should contain the nominal (true) value. In our previous work Naeimaei and Schön (2025), we derived deterministic uncertainty based on intervals in the observation domain (e.g., for range) and validated it using nominal values obtained from network adjustment. In many field campaigns (such as multi-station facades, tunnels, and dams), however, no trusted nominal value is available. This raises a practical question: how can interval bounds be validated *without* a nominal value?

This paper’s strategy is to work with *residuals*. Under a correctly specified LSA, residuals are zero in expectation; thus, zero serves as a nominal alternative in the residual domain. Consequently, interval radii are propagated to the residuals to ensure that zero is enclosed when averaging out the random variability. To establish interval uncertainty for the residuals, two practical issues must be addressed:

- **Model uncertainty.** Residuals can contain modelling error (e.g., fitting a plane to a slightly non-planar facade), which is difficult to separate from instrumental systematics.
- **Fixing model parameters.** Estimated parameters that describe the surface may absorb remaining systematic effects. To avoid this, model parameters should be fixed during the validation process.

This contribution has been peer-reviewed. The double-blind peer-review was conducted on the basis of the full paper.
https://doi.org/10.5194/isprs-annals-XI-1-2026-391-2026 | © Author(s) 2026. CC BY 4.0 License.

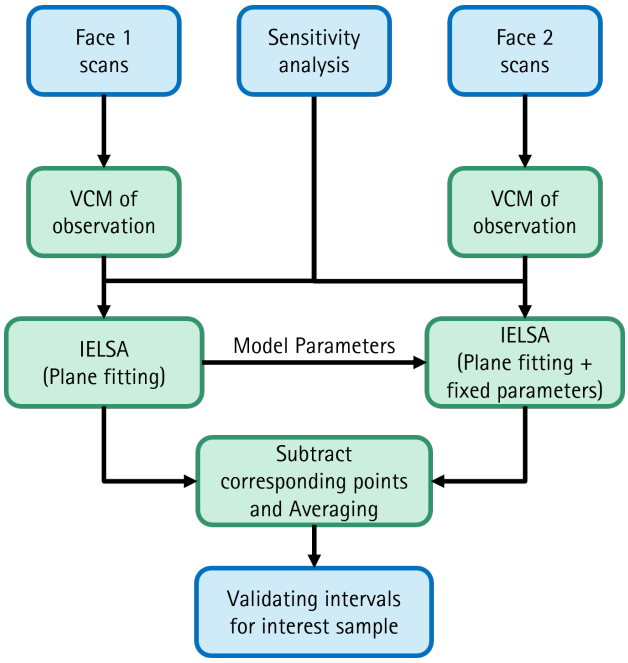

Figure 2. Flowchart for validating interval uncertainty via Interval-Extended Least-Squares Adjustment (IELSA) using two-face measurements.

To mitigate both effects, we use a two-face measurement design with the laser scanner. The workflow (Figure 2) involves estimating the scene model using Face 1 data, carrying the model parameters forward as hard constraints, and then evaluating the residuals using Face 2 data. Differencing between the two faces eliminates scene-model errors that are present in both and identifies sign-changing instrumental terms, while holding the parameters fixed prevents the absorption of systematics. The next sections detail the measurement model, the sensitivity analysis, and the extension of LSA to propagate intervals into the residual domain.

2.3 Measurement model for TLS

In TLS, Cartesian point coordinates are computed from polar measurements—range r, horizontal angle φ, and vertical angle θ—and their corrections:

$$\begin{bmatrix} x \\ y \\ z \end{bmatrix} = \begin{bmatrix} (r + C_r)\ \sin(\theta + C_\theta)\ \sin(\varphi + C_\varphi) \\ (r + C_r)\ \sin(\theta + C_\theta)\ \cos(\varphi + C_\varphi) \\ (r + C_r)\ \cos(\theta + C_\theta) \end{bmatrix}, \quad (1)$$

with (x, y, z) expressed in the scanner's coordinate system. This paper focuses on instrumental effects and models them through $(C_r, C_\varphi, C_\theta)$; other influences (e.g., atmosphere, object properties, scan geometry) are addressed in subsequent work.

The National Institute of Standards and Technology proposed a comprehensive correction model for instrumental error sources and a standard procedure for evaluating laser-scanner performance (Muralikrishnan et al., 2015). Medić et al. (2019) adapted a simplified version for high-end panoramic scanners and, from an initial set of 18 parameters, identified 10 dominant symmetric instrumental terms (Table 1). The corresponding corrections for range and angles are

$$C_r = x_2\ \sin\theta + x_{10}, \quad (2)$$

Table 1. Instrumental error–source parameters and calibration results (Medić et al., 2019).

Parameter	Description	Mean	Max. dev.
x_{1n} [mm]	Horizontal beam offset	0.05	0.07
x_{1z} [mm]	Vertical beam offset	0.19	0.23
x_2 [mm]	Horizontal axis offset	-0.12	0.03
x_3 [mm]	Mirror offset	-0.03	0.06
x_{10} [mm]	Rangefinder offset	-0.04	0.19
x_4 ["]	Vertical index offset	4.75	0.97
x_{5n} ["]	Horizontal beam tilt	5.04	1.12
x_{5z} ["]	Vertical beam tilt	-14.46	4.78
x_6 ["]	Mirror tilt	3.83	0.78
x_7 ["]	Horizontal axis error	-26.89	11.15

$$C_\varphi = \frac{x_{1n}}{r} + \frac{x_{1z}}{r\ \tan\theta} + \frac{x_3}{r\ \sin\theta} + \frac{x_{5z}}{\tan\theta} - \frac{x_7}{\tan\theta} + \frac{2x_6}{\sin\theta}, \quad (3)$$

$$C_\theta = \frac{x_{1n}\cos(\theta)}{r} + \frac{x_2\cos(\theta)}{r} + x_4 + x_{5n}\cos(\theta) - \frac{x_{1z}\sin(\theta)}{r} - x_{5z}\sin(\theta). \quad (4)$$

2.4 Sensitivity analysis

Sensitivity analysis quantifies how small changes in model inputs affect the output (BIPM et al., n.d.). Consider a scalar model $f(\mathbf{s})$ with n independent influence parameters $\mathbf{s} = \{s_i\}_{i=1}^n$. Linearizing f at a nominal point $\mathbf{s}^*$ yields

$$df = \sum_{i=1}^{n} \frac{\partial f(\mathbf{s}^*)}{\partial s_i}\, ds_i = \mathbf{F}\, \mathbf{ds}, \quad (5)$$

where $\mathbf{F}$ is the $1 \times n$ row vector of partial derivatives w.r.t the influence parameters evaluated at $\mathbf{s}^*$, while $\mathbf{ds}$ can be interpreted as their (possible or actual) deviation. In our context, f denotes a correction model from (2)–(4), and the s_i include influence parameters (Table 1).

2.5 Uncertainty propagation

The linearized model in (5) serves as the foundation for uncertainty propagation, which can be treated using different formalisms.

2.5.1 Stochastic Approach. If the input deviations ds_i are modeled as independent random variables with variances $\sigma_{s_i}^2$, the classical law of variance propagation gives the variance of the output f as:

$$\sigma_f^2 = \sum_{i=1}^{n} \left[\frac{\partial f(\mathbf{s}^*)}{\partial s_i}\right]^2 \sigma_{s_i}^2. \quad (6)$$

This stochastic approach captures random variability, typically under distributional assumptions (e.g., normal distribution).

2.5.2 Interval Approach. To concisely enclose *remaining systematic effects*, Kutterer (1999) employs an interval formulation. If each influential parameter is known to be bounded within an interval $s_i \in [\, s_i^* - \Delta_{s_i},\ s_i^* + \Delta_{s_i}\,]$, the maximum deviation (interval radius) of the output, Δ_f, is enclosed by:

$$\Delta_f = \sum_{i=1}^{n} \left|\frac{\partial f(\mathbf{s}^*)}{\partial s_i}\right| \Delta_{s_i} = |\mathbf{F}|\, \mathbf{\Delta}_s, \quad (7)$$

where $|\cdot|$ denotes the elementwise absolute value and $\boldsymbol{\Delta}_s$ is the vector of interval radii. In our context, $\boldsymbol{\Delta}_s$ is the maximum deviation of the parameters in Table 1. Applied to the correction models (2)–(4), let $\mathbf{F}$ be the Jacobians with respect to influential parameters. Then, the interval radii for observation $\boldsymbol{\Delta}_l := [\Delta_r, \Delta_\theta, \Delta_\varphi]^\mathsf{T}$ will be computed as

$$\boldsymbol{\Delta}_l \;=\; |\mathbf{F}|\,\boldsymbol{\Delta}_s, \tag{8}$$

It should be noted that we assume independence among influence parameters. While correlations may exist, this assumption ensures a strictly conservative upper bound for the uncertainty budget by modelling it as an axis-aligned box.

2.6 Interval-extended least-squares adjustment (IELSA)

Parameter estimation and residual analysis are formulated within the least-squares Gauss–Helmert model (GHM), which is standard in geodesy (see, e.g., Niemeier (2020); Malissiovas (2019)). To incorporate interval-based uncertainty, the Interval-Extended Least-Squares Adjustment (IELSA) concept of Kutterer (1999) is employed and transferred from its original Gauss–Markov setting to the GHM. This subsection links the linearized GHM Jacobians to the interval propagation derived in Sections 2.4–2.5.

2.6.1 Gauss–Helmert model (nonlinear form) The GHM is given by the implicit functional model

$$\mathbf{h}(\mathbf{L}+\mathbf{v},\,\mathbf{X}) = \mathbf{0}, \tag{9}$$

where $\mathbf{h} \in \mathbb{R}^n$ collects differentiable condition equations, $\mathbf{L} \in \mathbb{R}^m$ is the observation vector, $\mathbf{X} \in \mathbb{R}^u$ the parameter vector, and $\mathbf{v} \in \mathbb{R}^m$ the residual vector are assumed to be Gaussian $\mathbf{v} \sim \mathcal{N}(\mathbb{E}(\mathbf{v}), \boldsymbol{\Sigma}_{ll})$ with $\boldsymbol{\Sigma}_{ll} = \sigma_0^2 \mathbf{Q}_{ll}$, where $\mathbf{Q}_{ll}$ is the cofactor matrix and σ_0^2 the variance factor.

2.6.2 Linearization and Normal Equations Linearizing the implicit functional model (9) at the approximate solution $(\mathbf{v}^0, \mathbf{X}^0)$ yields

$$\mathbf{h}(\mathbf{L}+\mathbf{v},\,\mathbf{X}) \;=\; \mathbf{B}\,\mathbf{v} \;+\; \mathbf{A}\,\mathbf{x} \;+\; \mathbf{w} \;\stackrel{!}{=}\; \mathbf{0}, \tag{10}$$

with

$$\mathbf{A} = \left.\frac{\partial \mathbf{h}}{\partial \mathbf{X}}\right|_{(\mathbf{v}^0,\mathbf{X}^0)}, \qquad \mathbf{B} = \left.\frac{\partial \mathbf{h}}{\partial \mathbf{v}}\right|_{(\mathbf{v}^0,\mathbf{X}^0)}, \tag{11}$$

$$\mathbf{x} := \mathbf{X} - \mathbf{X}^0, \qquad \mathbf{w} := \mathbf{h}^0(\mathbf{L}+\mathbf{v}^0, \mathbf{X}^0) - \mathbf{B}\mathbf{v}^0. \tag{12}$$

Here, $\mathbf{A}$ and $\mathbf{B}$ are the Jacobian matrices with respect to the unknown parameters and the residuals, respectively. $\mathbf{x}$ is the parameter correction vector, and $\mathbf{w}$ is the misclosure vector.

A least squares solution is obtained by minimizing the objective function subject to the linear constraint (10).

$$\Omega(\mathbf{v}) = \mathbf{v}^\mathsf{T}\mathbf{P}\mathbf{v}, \quad \mathbf{P} = \mathbf{Q}_{ll}^{-1}. \tag{13}$$

Due to the implicit functional relationship between the parameters, this constrained optimization problem is solved using the method of Lagrange multipliers $\boldsymbol{\lambda}$ (see e.g. Bertsekas and Rheinboldt (2014); Förstner and Wrobel (2016)):

$$K(\mathbf{x}, \mathbf{v}, \boldsymbol{\lambda}) = \mathbf{v}^\mathsf{T}\mathbf{P}\mathbf{v} - 2\boldsymbol{\lambda}^\mathsf{T}(\mathbf{B}\mathbf{v} + \mathbf{A}\mathbf{x} + \mathbf{w}). \tag{14}$$

Setting the partial derivatives with respect to $\mathbf{x}$, $\mathbf{v}$, and $\boldsymbol{\lambda}$ to zero yields the symmetric block normal system

$$\begin{bmatrix} \mathbf{Q}_w & \mathbf{A} \\ \mathbf{A}^\mathsf{T} & \mathbf{0} \end{bmatrix} \begin{bmatrix} \widehat{\boldsymbol{\lambda}} \\ \widehat{\mathbf{x}} \end{bmatrix} = \begin{bmatrix} -\mathbf{w} \\ \mathbf{0} \end{bmatrix}, \qquad \mathbf{Q}_w := \mathbf{B}\mathbf{Q}_{ll}\mathbf{B}^\mathsf{T}. \tag{15}$$

Provided $\mathbf{Q}_w$ is not singular, the solution can be written (cf. Niemeier (2020))

$$\begin{bmatrix} \widehat{\boldsymbol{\lambda}} \\ \widehat{\mathbf{x}} \end{bmatrix} = \begin{bmatrix} \mathbf{Q}_{11} & \mathbf{Q}_{12} \\ \mathbf{Q}_{21} & \mathbf{Q}_{22} \end{bmatrix} \begin{bmatrix} -\mathbf{w} \\ \mathbf{0} \end{bmatrix}, \tag{16}$$

with

$$\mathbf{Q}_{22} = -\left(\mathbf{A}^\mathsf{T}\mathbf{Q}_w^{-1}\mathbf{A}\right)^{-1}, \quad \mathbf{Q}_{12} = -\mathbf{Q}_w^{-1}\mathbf{A}\mathbf{Q}_{22},$$
$$\mathbf{Q}_{21} = \mathbf{Q}_{12}^\mathsf{T}, \qquad\qquad \mathbf{Q}_{11} = \mathbf{Q}_w^{-1}(\mathbf{I}_m - \mathbf{A}\mathbf{Q}_{21})\,.$$

Explicitly,

$$\widehat{\mathbf{x}} = -\mathbf{Q}_{21}\mathbf{w} = -\left(\mathbf{A}^\mathsf{T}\mathbf{Q}_w^{-1}\mathbf{A}\right)^{-1}\mathbf{A}^\mathsf{T}\mathbf{Q}_w^{-1}\mathbf{w}, \tag{17}$$

$$\widehat{\boldsymbol{\lambda}} = -\mathbf{Q}_{11}\mathbf{w} = -\mathbf{Q}_w^{-1}(\mathbf{A}\widehat{\mathbf{x}} + \mathbf{w})\,, \tag{18}$$

$$\widehat{\mathbf{v}} = \mathbf{Q}_{ll}\mathbf{B}^\mathsf{T}\widehat{\boldsymbol{\lambda}} = -\mathbf{Q}_{ll}\mathbf{B}^\mathsf{T}\mathbf{Q}_{11}\mathbf{w}. \tag{19}$$

An iterative least-squares scheme updates

$$\mathbf{X}^0 \leftarrow \mathbf{X}^0 + \widehat{\mathbf{x}}, \qquad \mathbf{v}^0 \leftarrow \widehat{\mathbf{v}}, \tag{20}$$

until convergence. Cofactor matrices of the estimates follow as

$$\mathbf{Q}_{\widehat{x}\widehat{x}} = \left(\mathbf{A}^\mathsf{T}\mathbf{Q}_w^{-1}\mathbf{A}\right)^{-1}, \qquad \mathbf{Q}_{\widehat{v}\widehat{v}} = \mathbf{Q}_{ll}\mathbf{B}^\mathsf{T}\mathbf{Q}_{11}\mathbf{B}\mathbf{Q}_{ll}. \tag{21}$$

The estimated variance of the unit weight can be computed in this case by

$$\hat{\sigma}_0^2 = \frac{\hat{\mathbf{v}}^\mathsf{T}\mathbf{P}\,\hat{\mathbf{v}}}{dof}, \quad \text{with redundancy: } dof = n - u. \tag{22}$$

The VCM of the estimated corrections is obtained by scaling the corresponding cofactor matrix,

$$\boldsymbol{\Sigma}_{\hat{\mathbf{x}}\hat{\mathbf{x}}} = \hat{\sigma}_0^2\,\mathbf{Q}_{\hat{\mathbf{x}}\hat{\mathbf{x}}}. \tag{23}$$

2.6.3 Link to sensitivity-based uncertainty propagation To propagate the interval bounds from the influence-parameter domain to *residuals* and *parameters*, we first relate misclosures to observations. Following Niemeier (2020) after convergence, a first-order Taylor expansion of (12) with respect to $\mathbf{L}$ gives

$$\mathbf{w} = \underbrace{\mathbf{h}^0(\mathbf{L}^0 + \mathbf{v}^0, \mathbf{X}^0)}_{\mathbf{0}} + \left.\frac{\partial \mathbf{w}}{\partial \mathbf{L}}\right|_{\mathbf{L}=\mathbf{L}^0} \underbrace{(\mathbf{L} - \mathbf{L}^0)}_{\mathbf{l}} = \mathbf{J}_\mathbf{w}\,\mathbf{l}, \tag{24}$$

where $\mathbf{l}$ denotes the reduced observations and, as expected, the Jacobian with respect to $\mathbf{L}$ equals the Jacobian with respect to $\mathbf{v}$, i.e., $\mathbf{J}_\mathbf{w} = \mathbf{B}$.

Let $\mathbf{F}$ denote the Jacobian that maps deviations of influential parameters $\mathbf{s}$ to reduced observations $\mathbf{l}$. Using the interval bound $\boldsymbol{\Delta}_s$ from (8), the interval radii for the estimates follow by linear

mapping and elementwise absolute values:

$$\boldsymbol{\Delta}_{\hat{\mathbf{v}}} = \left| -\mathbf{Q}_{ll}\mathbf{B}^{\mathsf{T}}\mathbf{Q}_{11}\mathbf{B}\,\mathbf{F} \right| \boldsymbol{\Delta}_s, \tag{25}$$

$$\boldsymbol{\Delta}_{\hat{\mathbf{x}}} = \left| -\mathbf{Q}_{21}\mathbf{B}\,\mathbf{F} \right| \boldsymbol{\Delta}_s. \tag{26}$$

These expressions transfer the interval (bounded-error) description to the residual and parameter domains, providing conservative first-order bounds which show the remaining systematic error that complements the stochastic covariances in (21).

3. Experimental setup

This section describes the measurement strategy as well as the data acquisition and registration workflow used to validate the interval bounds.

3.1 Measurement strategy

We consider a large, approximately planar concrete structure, the *Bonn reference wall* (Figure 3). The wall is approximately $50\,\mathrm{m}$ wide and $10\,\mathrm{m}$ high (Schmitz et al., 2021). To enable residual-based validation using a two-face design, the wall was observed from five scanner stations, and at each station two scans were acquired in Face 1 and Face 2, yielding a total of 10 scans.

Panoramic TLS follow a total-station-like concept and therefore support *two-face* measurements: at a fixed station, the same surface is observed twice, once in Face 1 and once after a 180° transit in Face 2, i.e., with an inverted instrument orientation.

For target-based registration, thirteen artificial TLS targets (type BOTA8) were deployed in the scene. Target centers were estimated following (Janßen et al., 2019) and served as tie features for registration.

3.2 Data acquisition and registration

Data were collected using a high-end terrestrial laser scanner (Z+F Imager 5016). The wall was scanned with a point spacing (sampling interval) of $3.1\,\mathrm{mm}$ at a range of $10\,\mathrm{m}$; the effective resolving capability is additionally limited by the laser footprint/beam divergence. To minimize the influence of on-board filtering and proprietary processing, the lowest quality settings were selected during acquisition.

Registration was performed in Leica Cyclone using the target network, resulting in a root-mean-square (RMS) registration error of approximately $1\,\mathrm{mm}$ (Koller et al., 2025). The reference frame is defined by Station 5, Face 1; all other scans were rigidly aligned to this frame.

4. Experimental results

This section reports exemplarily the results obtained on a $1 \times 1\,\mathrm{m}$ patch of the Bonn reference wall (blue square in Figure 3). We first describe the plane-fitting model used to generate residuals, then validate the interval bounds in the residual domain, and finally discuss the results station-wise and observation-wise.

4.1 Coordinate Transformation and Plane-fitting Model

As described in Section 3, all scans were registered to a global reference frame (g) defined by Station 5, Face 1. For each scanner station $s \in \{1, \ldots, 5\}$ and face $f \in \{1, 2\}$, the registration

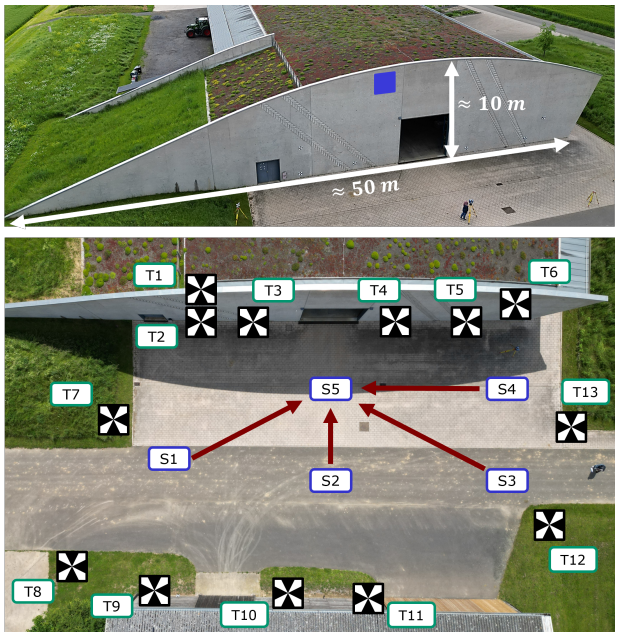

Figure 3. Bonn reference wall and acquisition geometry (five stations; two faces at each), and the interest sample is shown by a blue square.

yields a rotation $\mathbf{R}^{g}_{s,f} \in \mathrm{SO}(3)$ and a translation $\mathbf{t}^{g}_{s,f} \in \mathbb{R}^3$. Accordingly, the local scanner coordinates $\mathbf{p}^{l}$ are transformed to global coordinates $\mathbf{p}^{g}$ via:

$$\mathbf{p}^{g}_{s,f} = \mathbf{R}^{g}_{s,f}\,\mathbf{p}^{l}_{s,f} + \mathbf{t}^{g}_{s,f}. \tag{27}$$

Following the workflow in Figure 2, a plane was fitted in the global reference frame using all scans from Face 1 and Face 2. The plane is parameterized by a unit normal vector $\mathbf{n} = [\,n_x\ n_y\ n_z\,]^{\mathsf{T}}$ and an orthogonal distance to the origin $d \in \mathbb{R}$, leading to the implicit observation equation:

$$\mathbf{n}^{\mathsf{T}}\mathbf{p}^{g} - d = 0. \tag{28}$$

To remove the scale ambiguity inherent in the $(\alpha\mathbf{n}, \alpha d)$ representation, we divide by d (for $d \neq 0$). This yields the global-form observation equation used in our adjustment:

$$\underbrace{\frac{n_x}{d}}_{\bar{n}_x} x + \underbrace{\frac{n_y}{d}}_{\bar{n}_y} y + \underbrace{\frac{n_z}{d}}_{\bar{n}_z} z = 1, \qquad \bar{\mathbf{n}} = \frac{\mathbf{n}}{d}. \tag{29}$$

By using this scaled normal vector $\bar{\mathbf{n}}$, the plane is uniquely defined by three parameters, and the observation equation is simplified to $\bar{\mathbf{n}}^{\mathsf{T}}\,\mathbf{p}^{g} - 1 = 0$.

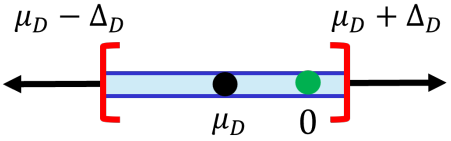

Figure 4. Validation concept in the residual domain. The combined interval radius Δ_D (light blue bar) is centered at the difference mean μ_D (black dot) and must enclose zero (green dot).

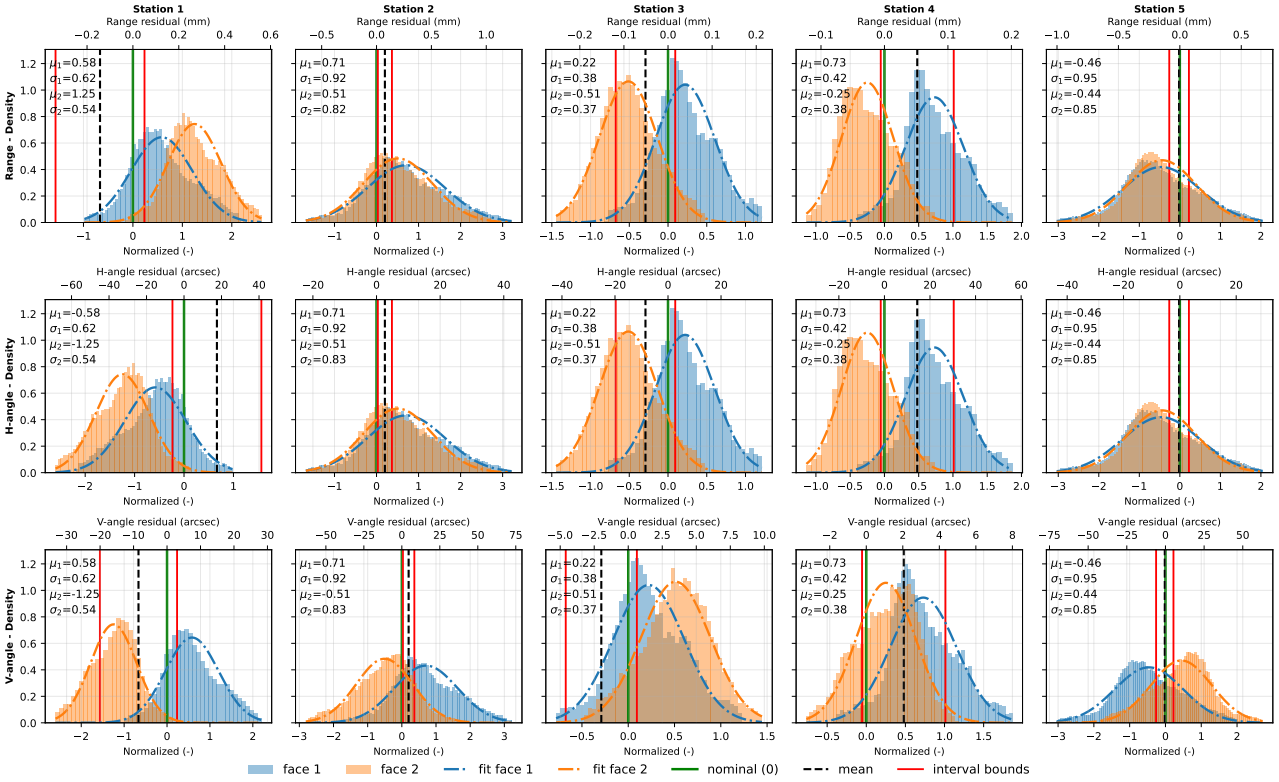

Figure 5. Validation across stations for the $1 \times 1\,\mathrm{m}$ patch: histograms of residuals (Face 1 in blue, Face 2 in orange), difference of means μ_D (black dashed), and combined interval bounds $\pm\Delta_D$ (red). Top axes show residuals in physical units (mm or arc-sec); bottom axes show normalized residuals (residual divided by its standard deviation, i.e., the square root of the corresponding diagonal of $\mathbf{Q}_{\widehat{v}\widehat{v}}$ in (21)).

4.2 Validation of interval uncertainty

Under a correctly specified adjustment and linearization about the mean observation vector, the estimated residuals are unbiased with zero expectation. We therefore treat zero as the nominal value in the residual domain and use the face-wise residual means as estimators against which the propagated interval bounds are validated.

Let $\widehat{\mathbf{v}}^{(1)}$ and $\widehat{\mathbf{v}}^{(2)}$ denote the residual vectors from Face 1 and Face 2, respectively, and define the *component-wise* sample means to average out random variability:

$$\mu_1 := \mathrm{mean}\big(\widehat{\mathbf{v}}^{(1)}\big), \qquad \mu_2 := \mathrm{mean}\big(\widehat{\mathbf{v}}^{(2)}\big). \tag{30}$$

To exploit the two-face design in a way that is consistent across components, we form a sign-aware face combination

$$\mu_D := \begin{cases} \mu_1 - \mu_2, & \text{if the face change preserves the sign,} \\ \mu_1 + \mu_2, & \text{if the face change flips the sign,} \end{cases}$$

equivalently, $\mu_D = \mu_1 - \eta\,\mu_2$ with $\eta \in \{+1, -1\}$. The choice of η is fixed *a priori* by the measurement model's sign convention for the corresponding residual component (not by the observed data): a face change preserves the sign for the range and horizontal-angle residuals, but flips the sign of the vertical-angle residual due to the geometric inversion of the vertical-circle reading. Hence we set $\eta = +1$ for range and horizontal angle and $\eta = -1$ for the vertical angle. With this definition, common model trends that appear with the same magnitude but opposite sign across faces are removed in μ_D.

From interval propagation (Section 2.6.3), let $\Delta^{(1)}_{\widehat{\mathbf{v}}}$ and $\Delta^{(2)}_{\widehat{\mathbf{v}}}$ denote the component-wise interval radii for the two faces. A conservative combined bound for the face combination is

$$\Delta_D = \max\big(\Delta^{(1)}_{\widehat{\mathbf{v}}} + \Delta^{(2)}_{\widehat{\mathbf{v}}}\big). \tag{31}$$

We form the validation interval (as shown in Figure 4)

$$I_D := [\,\mu_D - \Delta_D,\ \mu_D + \Delta_D\,]$$

and require that the nominal (zero) is enclosed:

$$0 \in I_D \quad \Longleftrightarrow \quad |\mu_D| \le \Delta_D. \tag{32}$$

In practice, μ_1, μ_2, and μ_D are computed from the residuals within the $1\,\mathrm{m} \times 1\,\mathrm{m}$ patch (Figure 3) and the criterion (32) is evaluated component-wise (range, horizontal angle, vertical angle). The overlaid Gaussian fits are close to the histograms, indicating near-normal residual behavior and supporting the stochastic part of the model.

4.3 Residual Assessment

Figure 5 summarizes, for each station (columns) and component (rows), the face-wise *normalized* residual histograms (Face 1: blue; Face 2: orange) with Gaussian fits, the sign-aware face combination μ_D (black dashed), the combined interval bounds $\pm\Delta_D$ (red), and the nominal at zero (green). The validation criterion $0 \in [\,\mu_D - \Delta_D,\ \mu_D + \Delta_D\,]$ (equivalently $|\mu_D| \le \Delta_D$) is satisfied across stations and components, confirming that the propagated interval bounds are appropriate in the residual domain.

This contribution has been peer-reviewed. The double-blind peer-review was conducted on the basis of the full paper.
https://doi.org/10.5194/isprs-annals-XI-1-2026-391-2026 | © Author(s) 2026. CC BY 4.0 License.

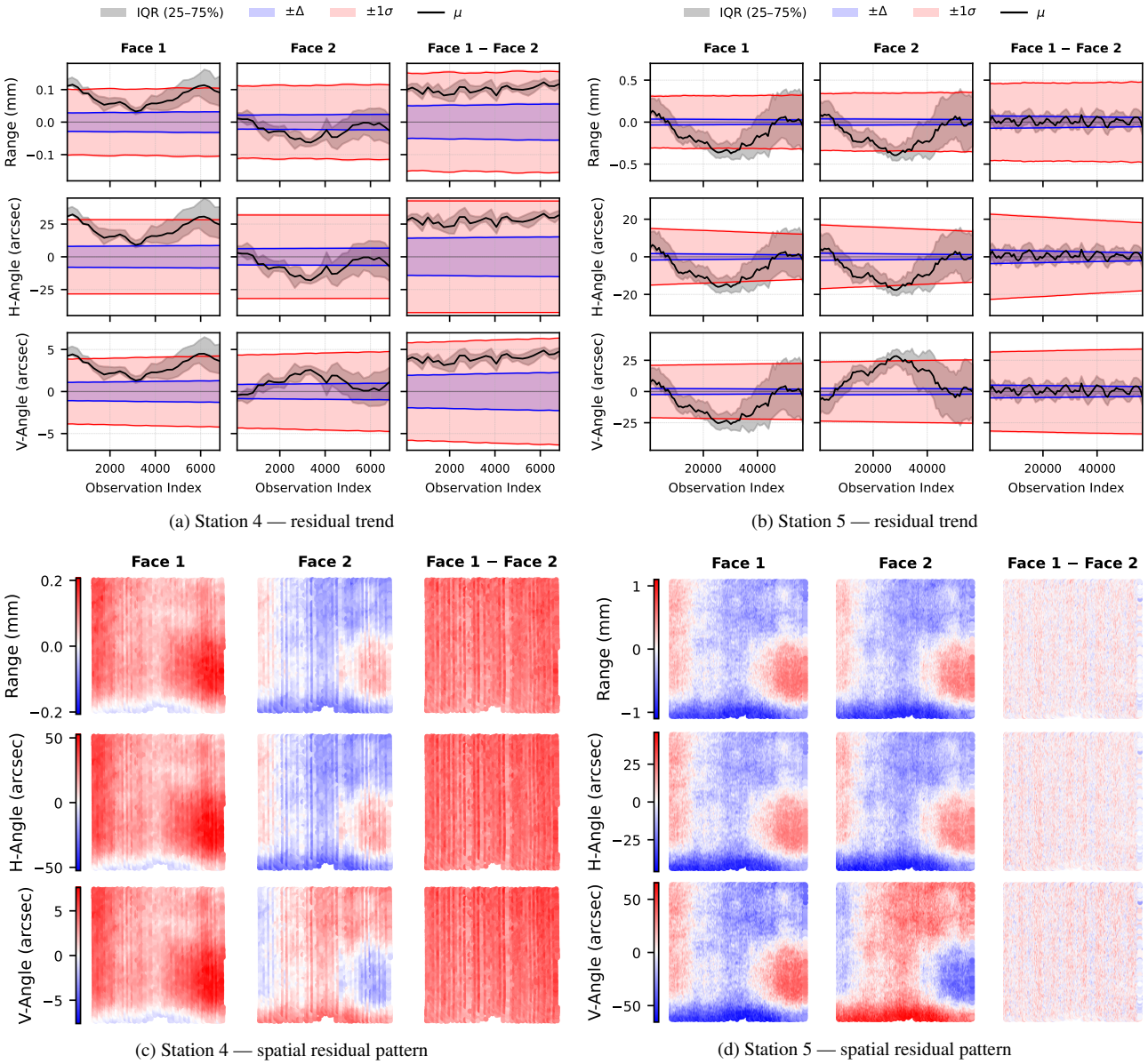

(a) Station 4 — residual trend

(b) Station 5 — residual trend

(c) Station 4 — spatial residual pattern

(d) Station 5 — spatial residual pattern

Figure 6. Residual trend and spatial pattern belong to Stations 4 and 5 by component (range, horizontal angle, vertical angle) for Face 1, Face 2, and the face difference. *Top row:* mean profile. *Bottom row:* corresponding spatial residual patterns.

Stations 1/3/4 exhibit the strongest face separation (modes shifted to opposite sides), yet the resulting μ_D remains enclosed by $\pm\Delta_D$. Stations 2/5 show closely aligned face means and therefore small $|\mu_D|$, with Station 2 lying closest to (and for the angle components marginally exceeding) the bounds, suggesting additional influences not yet covered by the current instrument-only interval budget. For the vertical angle, the sign-aware combination accounts for the face-dependent sign inversion, yielding μ_D values concentrated near zero and well within the bounds.

4.4 Analysis of Residual Trends and Spatial Patterns

This analysis intends to verify whether the derived interval bounds successfully enclose remaining systematic effects, distinguishing them from random noise. To realize this, we project face-combined residuals and their bounds onto the component-wise observations to visualize spatial patterns. This reveals whether violations are due to unmodeled instrumental drifts (which would appear as global trends) or external environmental factors (which appear as localized structures), thus serving as a diagnostic tool for the uncertainty budget.

4.4.1 Realization via Bin-wise Profiles and Spatial Mapping

Let $\{v_i\}_{i=1}^{n}$ denote a residual sequence (range or angles) in scan order. The index interval $[1, n]$ is partitioned into N_b equal-length bins with edges $\{e_k\}_{k=0}^{N_b}$ and centres $c_k = \frac{1}{2}(e_{k-1} + e_k)$; B_k denotes the indices in bin k and $|B_k|$ the cardinality of the set. The bin-wise mean and interquartile range (IQR) are

$$\mu_k = \frac{1}{|B_k|} \sum_{i \in B_k} v_i, \qquad \mathrm{IQR}_k = Q_{75\%,k} - Q_{25\%,k}, \tag{33}$$

where $Q_{p,k}$ is the pth percentile of $\{v_i\}_{i \in B_k}$. For the same bins, the interval and stochastic bands are

$$\Delta_k = \frac{1}{|B_k|} \sum_{i \in B_k} \Delta_i, \qquad \sigma_k = \frac{1}{|B_k|} \sum_{i \in B_k} \sigma_i. \tag{34}$$

In Figure 6 (a, b), μ_k is plotted as a black curve at c_k; the central 50% interval $[Q_{25\%,k}, Q_{75\%,k}]$ appears as a light-grey band; the interval band $\pm\Delta_k$ and the stochastic band $\pm 1\sigma_k$ are shown in blue and red, respectively.

To relate trends in scan order back to the object space, each residual v_i is additionally associated with its location on the $1\,\mathrm{m} \times 1\,\mathrm{m}$ wall patch. The residual field is then visualized in a spatial layout by mapping residuals to their corresponding positions on the patch (Face 1, Face 2, and the face-combined quantity) and displaying the resulting residual values as colour-coded images. This yields the spatial residual patterns shown in Figure 6 (c, d), which correspond to the profiles in (a, b) for Stations 4 and 5, respectively. Coherent spatial patches indicate localized effects (e.g., geometry-/registration-related contributions or surface-interaction effects), whereas near-uniform sign patterns over the patch are consistent with global drifts. The face-combined maps are expected to suppress common-mode contributions and thus provide a direct diagnostic of whether the remaining structure is face-dependent (instrument-related) or predominantly common to both faces.

4.4.2 Two-face combination and suppression of common–mode trends Residuals are combined per component according to the two-face symmetry of the measurement model as defined in Section 4.2. For range and horizontal angle, the face-combined mean profile is formed by differencing (Face 1 minus Face 2); for the vertical angle, a sign-aware combination is used to account for the face-dependent inversion introduced by the 180° transit. The corresponding combined uncertainty bands are

$$\Delta_{D,k} = \Delta_k^{(1)} + \Delta_k^{(2)}, \qquad \sigma_{D,k} = \sqrt{(\sigma_k^{(1)})^2 + (\sigma_k^{(2)})^2}.$$

This face combination reduces gentle trends and modelling contributions that are common to both faces, thereby emphasizing face-dependent effects when checking the enclosure of the face-combined mean against $\pm\Delta_{D,k}$.

Station 4. Face-specific profiles exhibit only mild drifts, and the face-combined series remains comfortably within $\pm\Delta_{D,k}$ for all components. The spatial maps show no persistent coherent structures, consistent with a clean validation outcome at this station.

Station 5. Face means are closely aligned, yet the spatial maps reveal localized coherent patches on the wall patch. In scan order, the face-combined profile approaches the interval band in short segments while remaining enclosed overall, reconciling the stable histogram behaviour with the presence of spatial structure. Such patterns indicate additional contributions that are largely common to both faces (e.g., scene-/geometry-dependent or registration-related effects) and motivate extending the interval budget beyond instrumental terms.

5. Conclusion and Outlook

This work presented an interval-based uncertainty framework for TLS that complements conventional VCM-based stochastic modelling. Using a sensitivity analysis of the TLS measurement and correction model, bounded deviations of influence parameters were propagated to observation-level intervals and integrated into a Gauss–Helmert adjustment via an interval-extended least-squares formulation. The result is a conservative first-order enclosure for residuals and parameter estimates alongside stochastic covariances.

A residual-domain validation strategy based on two-face acquisitions enables assessment without an external nominal reference: under a correctly specified adjustment and after averaging out random variability, the face-combined residual mean should be enclosed by the propagated interval bounds. For the $1\,\mathrm{m} \times 1\,\mathrm{m}$ patch of the Bonn reference wall, this enclosure holds across stations and components in general. Stations 1/3/4 show pronounced face separation yet remain enclosed, whereas Stations 2/5 exhibit closely aligned face means; Station 2 lies closest to the bounds for the angle components, indicating additional influences beyond the present instrument-only interval budget. For Station 5, the trend and spatial diagnostics reveal localized coherent structures despite overall enclosure, which points to scene-/geometry- or registration-related contributions that are largely common-mode but become visible in spatial analyses.

Future work will (i) extend the interval budget beyond instrumental parameters to include object properties, scan geometry, atmospheric effects, and registration uncertainty; (ii) exploit zonotopes to summarize combined effects in coordinate space; (iii) develop interval-extended statistical congruency tests that explicitly incorporate remaining systematic effects into the test decision, addressing the common limitation of purely stochastic (VCM-only) formulations in deformation monitoring; and (iv) investigate data-driven yet conservative calibration of interval radii to reduce pessimism while retaining guarantees.

Acknowledgements

This research was funded by the German Research Foundation (DFG) within the framework of the Research Unit FOR 5455: Deformation Analysis Based on Terrestrial Laser Scanner Measurements (TLS-Defo).

References

Alefeld, G., Herzberger, J., 1983. *Introduction to Interval Computations*. Academic Press, New York.

Bertsekas, D., Rheinboldt, W., 2014. *Constrained Optimization and Lagrange Multiplier Methods*. Computer science and applied mathematics, Academic Press.

BIPM, IEC, IFCC, ILAC, ISO, IUPAC, IUPAP, OIML, n.d. Guide to the expression of uncertainty in measurement — Part 1: Introduction. Joint Committee for Guides in Metrology, JCGM GUM-1:2023.

Caspary, W., Rüeger, J., of New South Wales. School of Surveying, U., 1987. *Concepts of Network and Deformation Analysis*. Monograph (University of New South Wales. School of Surveying), School of Surveying, University of New South Wales.

Förstner, W., Wrobel, B. P., 2016. *Photogrammetric Computer Vision*. Springer International Publishing.

Heunecke, Kuhlmann, H., Welsch, Eichhorn, Neuner, H., 2013. *Handbuch Ingenieurgeodäsie - Auswertung geodätischer Überwachungsmessungen*. neu bearbeitete und erweiterte Auflage.

Janßen, J., Medic, T., Kuhlmann, H., Holst, C., 2019. Decreasing the Uncertainty of the Target Center Estimation at Terrestrial Laser Scanning by Choosing the Best Algorithm and by Improving the Target Design. *Remote Sensing*, 11(7). https://www.mdpi.com/2072-4292/11/7/845.

Jaulin, L., Kieffer, M., Didrit, O., Walter, E., 2001. *Applied Interval Analysis with Examples in Parameter and State Estimation, Robust Control and Robotics*. Springer London.

Jost, B. H., 2023. Strategies for the Empirical Determination of the Stochastic Properties of Terrestrial Laser Scans. PhD thesis, Rheinische Friedrich-Wilhelms-University Bonn.

Kerekes, G., 2023. An elementary error model for terrestrial laser scanning. PhD thesis, Universität Stuttgart.

Koller, E., Jost, B., Kuhlmann, H., 2025. Towards the calibration of terrestrial laser scanners -a case study at a water dam.

Kuhlmann, H., Schwieger, V., Wieser, A., Niemeier, W., 2014. Engineering Geodesy - Definition and Core Competencies. *Journal of Applied Geodesy*, 8(4), 327–334. https://doi.org/10.1515/jag-2014-0020.

Kutterer, H., 1994. *Intervallmathematische Behandlung endlicher Unschärfen linearer Ausgleichungsmodelle*. Beck.

Kutterer, H., 1999. On the sensitivity of the results of least-squares adjustments concerning the stochastic model. *Journal of Geodesy*, 73, 350–361.

Malissiovas, G., 2019. New nonlinear adjustment approaches for applications in geodesy and related fields. PhD thesis, Dissertation, Fakultät VI–Planen Bauen Umwelt der Technische Universität Berlin.

Medić, T., 2021. Efficient calibration strategies for panoramic terrestrial laser scanners. PhD thesis, Rheinische Friedrich-Wilhelms-University Bonn.

Medić, T., Kuhlmann, H., Holst, C., 2019. Designing and evaluating a user-oriented calibration field for the target-based self-calibration of panoramic terrestrial laser scanners. *Remote Sensing*, 12(1), 15.

Moore, R. E., Kearfott, R. B., Cloud, M. J., 2009. *Introduction to Interval Analysis*. 110, SIAM, Philadelphia.

Muralikrishnan, B., Ferrucci, M., Sawyer, D., Gerner, G., Lee, V., Blackburn, C., Phillips, S., Petrov, P., Yakovlev, Y., Astrelin, A. et al., 2015. Volumetric performance evaluation of a laser scanner based on geometric error model. *Precision Engineering*, 40, 139–150.

Naeimaei, R., Schön, S., 2025. Interval-based Uncertainty Bounding for Terrestrial Laser Scanning Observations. *ISPRS Annals of the Photogrammetry, Remote Sensing and Spatial Information Sciences*, X-G-2025, 599–606. https://isprs-annals.copernicus.org/articles/X-G-2025/599/2025/.

Naeimaei, R., Schön, S., 2025. Deterministic uncertainty for terrestrial laser scanning observations based on intervals. *Journal of Applied Geodesy*, 19(3), 385–394. https://doi.org/10.1515/jag-2025-0034.

Niemeier, W., 2020. *Ausgleichungsrechnung*. De Gruyter Lehrbuch, reprint 2020 edn, De Gruyter, Berlin.

Reinhart, E., 1975. *Exakte Abschätzung von Maximalfehlern aus vorgegebenen Toleranzen der Beobachtungsgrößen*. Deutsche Geodätische Kommission, Reihe C, 211, Verlag der Bayerischen Akademie der Wissenschaften, München.

Schmitz, B., Kuhlmann, H., Holst, C., 2021. Deformation analysis of a reference wall towards the uncertainty investigation of terrestrial laser scanners. *Journal of Applied Geodesy*, 15(3), 189–206. https://doi.org/10.1515/jag-2020-0025.

Schön, S., Kutterer, H., 2006. Gps monitoring networks: interval-based description of measurement uncertainties due to remaining systematics. *Proc. 3rd IAG Symp. Geodesy for Geotechnical and Structural Engineering / 12th FIG Symposium on Deformation Measurements*, .

Su, J., Schön, S., 2022. Bounding the residual tropospheric error by interval analysis. *Geodesy for a Sustainable Earth: Proceedings of the 2021 Scientific Assembly of the International Association of Geodesy, Beijing, China, June 28–July 2, 2021*, Springer, 367–376.